High-pressure transformations in liquid rubidium

Simon Ayrinhac, Victor Naden Robinson, Frédéric Decremps, Michel Gauthier, Daniele Antonangeli, Sandro Scandolo, Marc Morand

High-pressure transformations in liquid rubidium

Simon Ayrinhac,[1] Victor Naden Robinson,[2] Frédéric Decremps,[1] Michel Gauthier,[1] Daniele Antonangeli,[1] Sandro Scandolo,[2] and Marc Morand[1]

[1]*Sorbonne Université, UMR CNRS 7590, Muséum National d'Histoire Naturelle, Institut de Minéralogie, de Physique des Matériaux et de Cosmochimie, IMPMC, 75005 Paris, France*

[2]*The "Abdus Salam" International Centre for Theoretical Physics, I-34151 Trieste, Italy*

(Received 3 August 2020; accepted 23 October 2020; published 30 November 2020)

An electronic-driven liquid-liquid phase transition in rubidium is revealed by picosecond acoustic measurements combined with *ab initio* calculations. Picosecond acoustics were used to measure the melting line up to 10 GPa, finding the maximum in the melting curve at 7 GPa and 555 K. We observe the onset of a continuous liquid-liquid phase transition beginning around the melting maxima through until 16 GPa. Sound velocity shows a softening similar to that reported for liquid caesium, caused by a change in the bulk modulus during a crossover from the low-density to the high-density liquid. Guided by the *ab initio* calculations, we relate the changes in the thermoelastic properties to the progressive localization of the valence electrons in the pressure range of 6–16 GPa. At high pressure rubidium forms an electride liquid quantified by the appearance of interstitial quasiatoms localized in the valence electron density.

DOI: 10.1103/PhysRevMaterials.4.113611

I. INTRODUCTION

Alkali metals are considered archetypal simple metals at ambient conditions yet exhibit complex properties at high pressure: Phase diagrams possess melting curves with several maxima (Cs [1]) and host-guest (h-g) incommensurate solid phases [2–5]. Light alkali metals become liquid at ambient temperature on compression to very high pressure (Li at 50 GPa [6], Na at 120 GPa [5]) or present a metal-insulator transition (Na becomes transparent at 200 GPa and ambient temperature [7]). Structural transformations in the liquid have been reported in Cs at 4 GPa and 493 K [8,9] and in Rb between 7.5 and 12.9 GPa at 573 K [10,11].

In parallel with the structural transformations, the electronic states of dense alkalis lose the free-electron metallic character in favor of orbital rehybridization and localization, leading to a reduction of metallicity and in the extreme case of Na even to the opening of a gap. Consensus is emerging, at least in light alkali metals, that electron localization is the result of the pressure-induced expulsion of valence electrons into the interstitial regions of the lattice leading to the formation of an electride state. The existence of electrides among solid alkali metals has been well established from pioneering [12,13] and more recent work [3,14–16]. Light alkali metals were first recognized to be electride solids at high pressure: Li at 60 GPa [16] and Na at 250 GPa [12]. Alkali metals which form complex h-g structures (Na, K, Rb) can be explained by their electride nature [3]. However, the effects are not as striking in heavy alkali metals. Moreover the presence of electrides remains to be confirmed and quantified for liquids.

At room temperature, solid Rb undergoes a series of transformations [17,18]: from bcc (Rb-I) to fcc (Rb-II) at 7 GPa [19], to Rb-III (*oC*52) at 13 GPa [20], to Rb-IV at 16 GPa (incommensurate h-g [21]) with an order-disorder transition [22] at 16.5 GPa, to Rb-V above 20 GPa (*tI*4) [19], and to Rb-VI around 50 GPa [23] (see Fig. 1). As is often the case, studies addressing the liquid are more controversial.

Early work interpreted anomalies of electrical conductivity and volume occurring on compression as signature of an electronic *s-d* transition [24,25]. A first-order liquid-liquid phase transition was suggested by *ab initio* molecular dynamics (AIMD) at 12.9 GPa and 573 K [10] on the basis of anomalies in the equation of state and the adiabatic coefficient, γ. Conversely, a gradual transition from a simple hard-sphere liquid to a complex liquid was recently proposed to occur in Rb at 7.5 ± 1 GPa [11] from measured x-ray diffraction (XRD). Measurements on heavy alkali metals are challenging due to their high reactivity, therefore thermodynamic data at high pressure p and temperature T is scarce or controversial (Cs [8,26,27] and Rb [10,11,28]).

Sound velocity measurements are a sensitive tool to detect structural transformations in the liquid state, such as Sn [29], Bi [30], Ga [31], or Cs [27]. Thus we perform picosecond acoustics (PA) measurements, a nondestructive technique well adapted to micrometric samples of liquid metals [32], inside a high-pressure diamond anvil cell (DAC). To investigate the microscopic origin of the anomalies observed by sound velocity measurements, AIMD simulations of the liquid were carried out, analyzing the structural and electronic changes. In this paper our combined experimental and computational study highlights an important structural transformation at 573 K from 6 GPa and extending up to 14 GPa resulting from the progressive change from the low-pressure free-electron-like liquid state to a high-pressure electride liquid.

II. METHODS

Picosecond acoustics is a time-resolved pump-probe optical technique that generates propagating strain waves in solids or liquids [31,32]. An 800-nm infrared laser pump pulse (100 fs width, 80 MHz repetition rate) is focused through a DAC at the surface of the metallic sample. The optically absorbed beam creates an acoustic strain pulse propagating across the sample, which is then detected at the opposite surface by a probe beam. The acoustic echoes induce changes in the refractive index of the liquid metal and displacement of the surface, which are measured by relative reflectivity variations seen with the probe beam. These surface reflections are used both to determine the travel time of the acoustic echoes, and hence sound velocity, and to identify melting as they strongly depend on the long-range order of the material [29,31] (see Supplemental Material [33] for details).

A sample chipped out from a Rb ingot (99.6% purity Sigma Aldrich [33]) was loaded into a hole drilled in a rhenium gasket inside the DAC. To minimize chemical contamination and reaction with air, the loading was performed in a glove box (<5 ppm O_2, H_2O). The pressure was measured by the shift of the temperature-independent fluorescence band of a SrB_4O_7:5%Sm^{2+} gauge placed in the sample chamber to act as a pressure calibrant [34]. Pressure determination from the internal pressure gauge is compared to the estimation from the high-frequency edge of the diamond-anvil Raman signal measured at the center of the gasket hole [35].

Due to unknown stress distribution inside the diamond anvils, the P scale was corrected to known pressure points (ambient pressure if reached, for example). High temperature was generated by a calibrated resistive heater surrounding the DAC. The adiabatic sound velocity v_s is obtained dividing the gasket thickness (around 20 μm) by the time of flight of the propagating acoustic strain wave. To ensure the hole thickness remained constant [36,37], measurements were made during sample decompression with a fine DAC membrane control (0.05 bar/min).

Density-functional theory calculations utilized the CASTEP code [38], using the generalized-gradient approximated exchange correlation [39], and a nine-electron ultrasoft pseudopotential with 2.1-bohr inner-core radius. A 300-eV plane-wave cutoff was used in AIMD with k points sampled at the Γ point. For solids, a grid density of 0.02 $Å^{-1}$ was used for structure optimization in agreement with Ref. [3]. Simulations ran at fixed density with a Nose-Hoover thermostat starting from a 128-atom melted bcc supercell quenched down to either 573 or 800 K. The liquid was simulated up to 30 ps along the 573 and 800 K isotherms with a 0.75-fs time step and sampling the stress tensor every 10 steps.

After liquid equilibration, the mean internal energy, U, was used to determine isochoric specific heat, $C_V = (\frac{\partial U}{\partial T})_V$. The isothermal compressibility, $\beta_T = \frac{1}{V}(\frac{\partial V}{\partial P})_T$, where V is the molar volume, was computed from the AIMD equation of state. The thermal expansion coefficient was calculated by $\alpha = \beta_T(\frac{\partial P}{\partial T})_V$, and isobaric specific heat, C_p, was determined from Mayer's relation $C_p = C_V + VT\beta_T^{-1}\alpha^2$. From the adiabatic ratio, $\gamma = C_p/C_V$, the adiabatic sound velocity, v_S, can be computed with $v_S = \sqrt{\gamma/\rho\beta_T}$ where ρ is the density.

III. RESULTS

The melting curve of Rb is well known below 7 GPa [42–44] but remains debated at higher pressures. As illustrated in the phase diagram shown in Fig. 1 inconsistencies exist amongst available experimental data: The liquid-solid transition at 618 K from Lundegaard [22] appears at 17 GPa, as opposed to 24 GPa by Gorelli *et al.* [11], yet both were determined by XRD. Here melting was detected using PA by imaging changes in wavefront patterns appearing at the sample surface [31]: Perfect circles indicate a liquid sample, whereas more complex patterns are observed in solid phases [33]. In addition, in liquid phase, the signal is less noisy or disturbed, and the position of the echo peak shifts due to variation of sound velocity between solid and liquid phases. Determination of the solid and melted states up to 10 GPa confirm the first maximum at 7 GPa and 555 K and are in good agreement with Kechin *et al.* [40] and Boehler and Zha [41].

The phase diagram and the pressure evolution of the liquid sound velocity (see Fig. 2) of Rb are both similar to that of Cs suggesting a double maximum in the melting line as already proposed by Boehler and Zha [41]. However, data beyond 10 GPa are limited: The thesis of Lundegaard reports molten Rb at 3 *p-T* points [45], in overall agreement with the low-temperature melting line suggested by Boehler and Zha [41], in spite of possible problems of sample contamination occurring above 10 GPa. This thesis also contains unpublished liquid structure factors of Rb around 10, 13, 18 GPa [33].

In the liquid, we probed the adiabatic sound velocities along the 573 K isotherm, systematically observing in the multiple performed runs an anomalous behavior (Fig. 2).

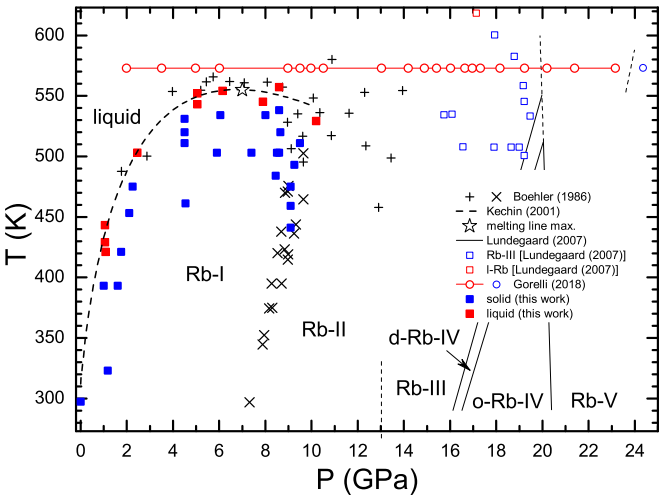

FIG. 1. Phase diagram of Rb: Solid (blue squares) and liquid (red squares) phases were detected using PA. The melting line is shown up to 10 GPa (dashed line) according to the functional form given by Kechin [40]. The melting maximum is at 7 GPa, 555 K (empty star). Transitions from bcc to fcc (crosses) and melting (pluses) are from Boehler [41]. Data at high *p-T* [11,22,41] is scarce and not always consistent. Sound velocity measurements in this work were performed along the 573 K isotherm as in Gorelli *et al.* [11] (red circles).

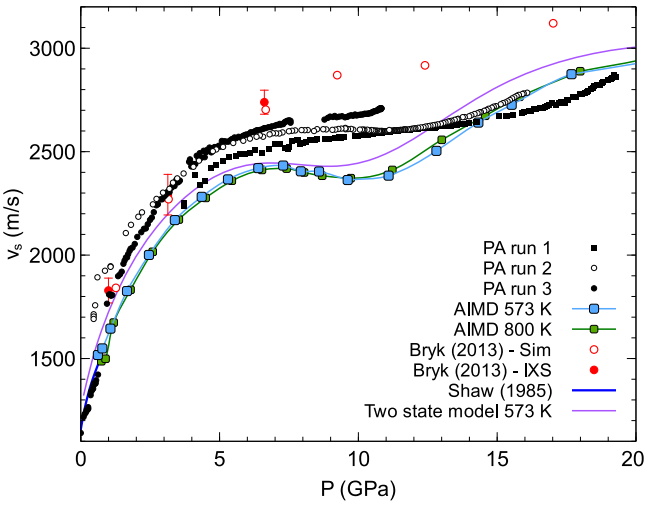

FIG. 2. Adiabatic sound velocities of liquid rubidium at 573 K as a function of pressure, measured by PA (black points), AIMD simulations (blue squares), and a two-state thermodynamic model (magenta) [33]. For comparison, ultrasonic measurements are shown from Shaw *et al.* [46] to 0.7 GPa and the AIMD and IXS measurements from Bryk *et al.* [10].

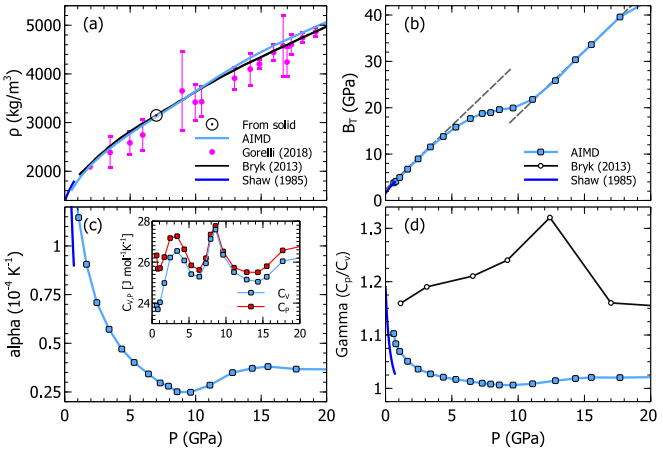

FIG. 3. Thermodynamic properties of liquid Rb at 573 K as a function of pressure including literature data from Gorelli [11] (XRD, pink), Bryk [10] (AIMD, black), and Shaw [46] (from ultrasonic measurements, blue). (a) Density; at the maxium of melting curve, the density of the solid (open dotted circle) is equal to that of the liquid. (b) Isothermal bulk modulus B_T with dashed lines to guide the eye. (c) Thermal expansivity; inset: Specific heat capacities. (d) Adiabatic ratio $\gamma = C_p/C_V$.

Plateaus were found in v_s between 6 and 14 GPa in experimental runs 1 and 3, while run 2 and AIMD (573, 800 K) found an oscillation in this region similar to the N-shape observed in liquid Cs [27]. A simple two-state model, which describes a system of entities in two thermodynamic states [47], in this case the two liquids, also finds an oscillation as the liquids mix. While PA measurements do not provide highly accurate absolute value of v_S due to the uncertainty on sample thickness ($\Delta v_S \simeq \pm 100$ m/s), our results agree closely with the data of Shaw [46] to 0.7 GPa and inelastic X-ray scattering (IXS) determinations from Bryk [10] to 6 GPa. At pressures over 6 GPa we find that PA and AIMD both have a lower v_s than the simulations of Bryk, where PA data appears between the v_s profiles of Bryk and AIMD performed in this work.

IV. DISCUSSION

As is clear from the change in the Clapeyron slope, the liquid becomes denser than the solid after the first melting line maxima at about 7 GPa, and the v_s plateau starts from this pressure. The complex, dense, phases of solid Rb (III, IV, and V) become stable around 14 GPa, pressure above which v_s starts again to rise with increasing pressure. We thus interpret the anomalous pressure evolution of the adiabatic velocity as a direct consequence of a continuous but rapid transformation between two distinct microscopic states of the liquid. As shown in Fig. 3, while density does not show any sharp discontinuity in the transition region, where two states coexist, the bulk modulus shows a plateau, directly related to the plateau of the sound velocity. Conversely, sound velocity shows no evidence for anomalies due to a second transition expected at 12.9 GPa according to Bryk [10].

Thermodynamic properties of liquid Rb are summarized in Fig. 3 which show no indications of a first- or second-order phase transition, suggesting that this is a gradual crossover between two types of liquid. Density was obtained from AIMD simulations showing agreement with previous experimental and computational determinations [10,11]. A small inflection is visible around 8–9 GPa in correspondence to the anomalous sound velocity. The density of the bcc solid at 7 GPa, corresponding to the maximum in the melting curve, is 3140 ± 20 kg/m^3 [33] in agreement with the density of the liquid as from AIMD and data of Bryk. The density of AIMD in this work is slightly lower than that of Bryk below 9 GPa but significantly greater beyond 12 GPa. To 0.7 GPa the density was calculated by a numerical procedure [31] from the accurate adiabatic sound velocity data of Shaw [46] extrapolated to 573 K, consistent with AIMD. The isothermal bulk modulus, related to density by $B_T = \rho(\partial p/\partial \rho)_T$, reveals a transition between two clear profiles as illustrated in Fig. 3(b). Thermal expansivity [Fig. 3(c)] exhibits a minima between 7 and 14 GPa which is also expected by the two-state model, and the specific heat capacities appear to have local maxima and minima in this pressure region. The adiabatic ratio, Fig. 3(d), shows a decreasing trend with pressure similar to other compressed liquids (H_2 [48], K [49]), but in contrast to results from Bryk, who reported much higher values, and argued for a discontinuity at 12.9 GPa not supported by our calculations. In fact, such high values of gamma would yield even greater sound velocities with a discontinuity if computed with the compressibility from AIMD in this work.

As is clear from the bulk modulus, liquid Rb is highly compressible at ambient conditions ($B_0 = 1.54$ GPa), with a B_0 value comparable with noble-gas solid Ne [50] ($B_0 = 1.07$ GPa), and by 5 GPa $V/V_0 = 0.5$. At this compression ratio two Rb^+ ions are so close (3.86 Å) that the valence shell (radius of 2.44 Å) of one overlap with the impenetrable ion core of the nearest other (radius of 1.48 Å), pushing the conduction electrons to migrate inside voids between ion cores. An electronic localization starts to occur around 6 GPa

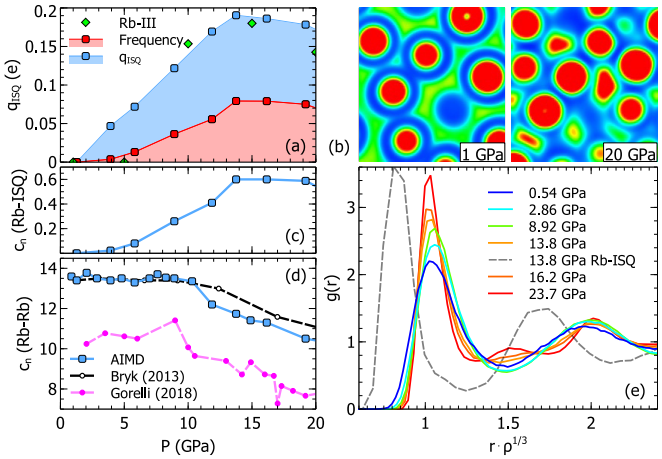

FIG. 4. Electronic and structural properties of liquid Rb as a function of pressure at 573 K. (a) Average charge inside interstitial Bader maxima (blue) and their frequency (red) per Rb ion. (b) Electron localization function (max = 0.70) 100 cuts from AIMD snapshots at 1 and 20 GPa showing localized interstitial charge (yellow to red amorphous shapes) appear between ions (red circles). (c) Coordination numbers for Rb ions to ISQs calculated by integrating PDFs up to the first minima and (d) for Rb-Rb ions. (e) Normalized Rb-Rb PDFs at selected pressures showing the first minima evolve into a new maxima, and a Rb-ISQ PDF at 13.8 GPa demonstrates the interstitial occupation of electride sites.

[see Fig. 4(a)], when a fraction of valence electrons start becoming confined in spaces between the ion cores, producing interstitial quasiatoms (ISQs) [16].

The localization is evident in AIMD snapshots comparing the interstitial electron localization at 1 and 20 GPa in Fig. 4(b). ISQs were detected as off-atom maxima in a Bader analysis of the electron density [51] averaged over 100 snapshots at selected pressures [see Fig. 4(a)]. From 6 GPa, the number of ISQ (and their total charge) increase with pressure [see Fig. 4(a)] to 0.2 e/ISQ around 14 GPa, where Rb-III and Rb-IV become stable. Compared to liquid Rb, in Rb-IV 0.3 e/ISQ were found at 20 GPa in the Bader scheme but around 1.1 e/ISQ when integrating electron localization function (ELF) basins [3], suggesting that the value in the liquid may be three times higher if ELF basins were integrated instead (to 0.6 e/ISQ at 14 GPa). The build up of electron localization with pressure was noted by Bryk [10] presenting three-dimensional ELF isosurfaces. A comparison with the liquid and solid phases of Rb to 50 GPa, and the distribution of charge within ISQs in the liquid, is shown in [33]. The Rb-Rb coordination number c_n drops from 10/11 GPa to around 8 [see Fig. 4(d)] which is when the ISQ's have significantly asserted their presence in the liquid. The decrease in c_n is suggested, in analogy to the liquid-liquid transformation in Cs [8,9], though the author stresses that higher-quality structural data are required to determine the nature of the high- and low-density liquids.

Miao *et al.* showed that for solids above 10 GPa the "Rb 5s" valence orbital is favored to form an "ISQ 1s" state (see Fig. 5 of Ref. [14]). Here Rb is able to access these states already from 6 GPa as the liquid is not restricted by symmetry. The creation of more ISQs, containing a fractional charge, attract Rb^+ ions and offer additional screening of interactions which can reduce the internal energy and cause a deepening of the attractive part of the potential. This can cause the softening evidenced in both the isothermal bulk modulus and sound velocity.

Density-normalized pair distribution functions (PDFs) [Fig. 4(e)] show a simple Lennard-Jones liquid structure at low P, and the apparition of an intermediate coordination shell between 8.9 and 13.8 GPa in conjunction with the continuous decrease of coordination number similar to Cs [9]. The thesis of Lundegaard eluded the similar transformation in liquid Cs [8,9] in the measured structure factor S(q), suggesting a decrease in the coordination number (c_n drops to around 8), though the author stresses that higher-quality structural data are required to determine the nature of the high- and low-density liquids.

From 10/11 GPa, coordination number between Rb ions starts decreasing following the trend observed in solid phases: $c_n = 14$ in Rb-I (bcc), 12 in Rb-II (fcc), 8/9 in RB-III (oc52), 9 in Rb-IV (*h*-*g*), and 8 in Rb-V (*tI*4). The coordination numbers measured by Gorelli [11] also decrease above 10 GPa but are significantly lower than AIMD. Similarly, their PDFs [33] have much broader first peaks compared to AIMD results discussed here and of Bryk [10]. Lower coordination indicates an open structure, likely due to creation of directional bonds between Rb^+ cations and ISQ anions [15], creating a "complex" liquid, with a structure similar to the high-pressure solid phases mediated by the localized electrons.

V. CONCLUSION

In summary, we mapped the phase diagram of Rb at high-pressure probing melting and a liquid-liquid transition through sound velocity measurements and used *ab initio* simulations to understand the nature of this transition. The Rb melting line was accurately measured to 10 GPa by picosecond acoustic techniques, clearly showing a maximum at 7 GPa. Multiple experiments found a progressive pressure-induced transformation in liquid Rb, highlighted by a plateau in the sound velocity between 6 and 14 GPa, while AIMD simulations similarly found an oscillation over the same pressure range. This anomaly is caused by an increase of compressibility concomitant to a continuous transition between two microscopically distinct states of the liquid. Absence of discontinuities in the density and compressibility clearly indicate that the phase transition is neither first nor second order, as claimed by previous work, but a crossover. The transition is related to a progressive localization of the electrons in interstitial regions as Rb forms a complex weak electride liquid. This is as well in stark contrast to previous explanations of 5*s* electrons occupying the 4*d* band, as partial density of states calculations can misinterpret electride materials, similarly shown for the solid alkali metals [3]. The maximum in the melting line requires the liquid to be less dense than the solid below 7 GPa and denser than the solid above 7 GPa. Macroscopically the liquid continuously take on properties of the high-pressure phases (thermodynamically stable after the melting minima). The properties of the complex solid phases, including structural transformations and electride character, are mirrored in the liquid, as they are continuously adopted,

with an extended transition region as the liquid-liquid transition mixes the two types of liquids.

ACKNOWLEDGMENTS

We thank H. Moutaabbid for his supporting help on the glove box and G. Le Marchand, Y. Guarnelli, and P. Parisiadis for their support on high-pressure devices. D.A. has received funding from the European Research Council (ERC) under the European Union's Horizon 2020 research and innovation Programme (Grant No. 724690). Authors warmly thank Y. Garino, P. Rosier, and N. Dumesnil for their strong implication on the current picosecond acoustics set-up upgrade.

[1] A. Jayaraman, R. C. Newton, and J. M. McDonough, Phys. Rev. **159**, 527 (1967).
[2] E. E. McBride, K. A. Munro, G. W. Stinton, R. J. Husband, R. Briggs, H.-P. Liermann, and M. I. McMahon, Phys. Rev. B **91**, 144111 (2015).
[3] G. Woolman, V. Naden Robinson, M. Marqués, I. Loa, G. J. Ackland, and A. Hermann, Phys. Rev. Materials **2**, 053604 (2018).
[4] V. N. Robinson, H. Zong, G. J. Ackland, G. Woolman, and A. Hermann, Proc. Natl. Acad. Sci. USA **116**, 10297 (2019).
[5] E. Gregoryanz, L. F. Lundegaard, M. I. McMahon, C. Guillaume, R. J. Nelmes, and M. Mezouar, Science **320**, 1054 (2008).
[6] C. L. Guillaume, E. Gregoryanz, O. Degtyareva, M. I. McMahon, M. Hanfland, S. Evans, M. Guthrie, S. V. Sinogeikin, and H. Mao, Nat. Phys. **7**, 211 (2011).
[7] Y. Ma, M. Eremets, A. R. Oganov, Y. Xie, I. Trojan, S. Medvedev, A. O. Lyakhov, M. Valle, and V. Prakapenka, Nature **458**, 182 (2009).
[8] S. Falconi, L. F. Lundegaard, C. Hejny, and M. I. McMahon, Phys. Rev. Lett. **94**, 125507 (2005).
[9] S. Falconi and G. J. Ackland, Phys. Rev. B **73**, 184204 (2006).
[10] T. Bryk, S. De Panfilis, F. A. Gorelli, E. Gregoryanz, M. Krisch, G. Ruocco, M. Santoro, T. Scopigno, and A. P. Seitsonen, Phys. Rev. Lett. **111**, 077801 (2013).
[11] F. A. Gorelli, S. De Panfilis, T. Bryk, L. Ulivi, G. Garbarino, P. Parisiades, and M. Santoro, J. Phys. Chem. Lett. **9**, 2909 (2018).
[12] J. B. Neaton and N. W. Ashcroft, Phys. Rev. Lett. **86**, 2830 (2001).
[13] B. Rousseau and N. W. Ashcroft, Phys. Rev. Lett. **101**, 046407 (2008).
[14] M.-S. Miao and R. Hoffmann, Acc. Chem. Res. **47**, 1311 (2014).
[15] M.-s. Miao and R. Hoffmann, J. Am. Chem. Soc. **137**, 3631 (2015).
[16] M.-S. Miao, R. Hoffmann, J. Botana, I. I. Naumov, and R. J. Hemley, Angew. Chem. **129**, 992 (2017).
[17] H. Olijnyk and W. Holzapfel, Phys. Lett. A **99**, 381 (1983).
[18] M. Winzenick, V. Vijayakumar, and W. B. Holzapfel, Phys. Rev. B **50**, 12381 (1994).
[19] V. F. Degtyareva, Solid State Sci. **36**, 62 (2014).
[20] R. J. Nelmes, M. I. McMahon, J. S. Loveday, and S. Rekhi, Phys. Rev. Lett. **88**, 155503 (2002).
[21] U. Schwarz, A. Grzechnik, K. Syassen, I. Loa, and M. Hanfland, Phys. Rev. Lett. **83**, 4085 (1999).
[22] L. F. Lundegaard, High-pressure diffraction studies of rubidium phase IV, Ph.D. thesis, University of Edinburgh, 2007.
[23] U. Schwarz, K. Syassen, A. Grzechnik, and M. Hanfland, Solid State Commun. **112**, 319 (1999).
[24] S. M. Stishov and I. N. Makarenko, Zh. Eksp. Teor. Fiz. **54**, 708 (1968) [Sov. Phys. JETP **27**, 378 (1968).
[25] I. N. Makarenko, V. A. Ivanov, and S. M. Stishov, JETP Lett. **18**, 187 (1973).
[26] T. Hattori, Phys. Rev. B **97**, 100101(R) (2018).
[27] F. Decremps, S. Ayrinhac, M. Gauthier, D. Antonangeli, M. Morand, Y. Garino, and P. Parisiades, Phys. Rev. B **98**, 184103 (2018).
[28] I. Loa, L. F. Lundegaard, M. I. McMahon, S. R. Evans, A. Bossak, and M. Krisch, Phys. Rev. Lett. **99**, 035501 (2007).
[29] L. Xu, Y. Bi, X. Li, Y. Wang, X. Cao, L. Cai, Z. Wang, and C. Meng, J. Appl. Phys. **115**, 164903 (2014).
[30] M. Emuna, M. Mayo, Y. Greenberg, E. Caspi, B. Beuneu, E. Yahel, and G. Makov, J. Chem. Phys. **140**, 094502 (2014).
[31] S. Ayrinhac, M. Gauthier, G. L. Marchand, M. Morand, F. Bergame, and F. Decremps, J. Phys.: Condens. Matter **27**, 275103 (2015).
[32] F. Decremps, M. Gauthier, S. Ayrinhac, L. Bove, L. Belliard, B. Perrin, M. Morand, G. Le Marchand, F. Bergame, and J. Philippe, Ultrasonics **56**, 129 (2015).
[33] See Supplemental Material at http://link.aps.org/supplemental/10.1103/PhysRevMaterials.4.113611 for details on the experimental data analysis (Secs. 1-2), the two-state thermodynamic model (Sec. 3), the thermodynamic parameters (Sec. 5), and the data obtained by AIMD simulations [structure factors and pair distribution functions (Sec. 4), interstitial quasi-atoms (Sec. 6), equation of state and diffusion coefficient (Sec. 7)].
[34] F. Datchi, A. Dewaele, P. Loubeyre, R. Letoullec, Y. Le Godec, and B. Canny, High Press. Res. **27**, 447 (2007).
[35] S. Ono, K. Mibe, and Y. Ohishi, J. Appl. Phys. **116**, 053517 (2014).
[36] A. Dewaele, J. H. Eggert, P. Loubeyre, and R. Le Toullec, Phys. Rev. B **67**, 094112 (2003).
[37] S. Ayrinhac, M. Gauthier, L. E. Bove, M. Morand, G. L. Marchand, F. Bergame, J. Philippe, and F. Decremps, J. Chem. Phys. **140**, 244201 (2014).
[38] S. J. Clark, M. D. Segall, C. J. Pickard, P. J. Hasnip, M. I. J. Probert, K. Refson, and M. C. Payne, Z. Kristallogr. **220**, 567 (2005).
[39] J. P. Perdew, K. Burke, and M. Ernzerhof, Phys. Rev. Lett. **77**, 3865 (1996).
[40] V. V. Kechin, Phys. Rev. B **65**, 052102 (2001).
[41] R. Boehler and C.-S. Zha, Physica B+ C **139**, 233 (1986).
[42] H. Luedemann and G. Kennedy, J. Geophys. Res. **73**, 2795 (1968).
[43] A. Nikolaenko, I. Makarenko, and S. Stishov, Solid State Commun. **27**, 475 (1978).

[44] R. Boehler and D. Young, J. Non-Cryst. Solids **61**, 141 (1984).
[45] L. F. Lundegaard, Ph.D. thesis, University of Edinburgh, 2007.
[46] G. H. Shaw and D. A. Caldwell, Phys. Rev. B **32**, 7937 (1985).
[47] V. Holten and M. A. Anisimov, Sci. Rep. **2**, 713 (2012).
[48] K. Matsuishi, E. Gregoryanz, H.-k. Mao, and R. J. Hemley, J. Chem. Phys. **118**, 10683 (2003).
[49] H. Li, H. Ding, Y. Tian, Y. L. Sun, and M. Li, AIP Adv. **9**, 075018 (2019).
[50] A. Dewaele, F. Datchi, P. Loubeyre, and M. Mezouar, Phys. Rev. B **77**, 094106 (2008).
[51] S. G. Dale and E. R. Johnson, J. Phys. Chem. A **122**, 9371 (2018).